

Article

Atmospheric Turbulence Effects on Wind-Turbine Wakes: An LES Study

Yu-Ting Wu and Fernando Porté-Agel *

Wind Engineering and Renewable Energy Laboratory (WIRE), École Polytechnique Fédérale de Lausanne (EPFL), EPFL-ENAC-IIE-WIRE, Lausanne CH-1015, Switzerland;

E-Mail: yu-ting.wu@epfl.ch

* Author to whom correspondence should be addressed; E-Mail: fernando.porte-agel@epfl.ch.

Received: 10 October 2012; in revised form: 28 November 2012 / Accepted: 11 December 2012 /

Published: 17 December 2012

Abstract: A numerical study of atmospheric turbulence effects on wind-turbine wakes is presented. Large-eddy simulations of neutrally-stratified atmospheric boundary layer flows through stand-alone wind turbines were performed over homogeneous flat surfaces with four different aerodynamic roughness lengths. Emphasis is placed on the structure and characteristics of turbine wakes in the cases where the incident flows to the turbine have the same mean velocity at the hub height but different mean wind shears and turbulence intensity levels. The simulation results show that the different turbulence intensity levels of the incoming flow lead to considerable influence on the spatial distribution of the mean velocity deficit, turbulence intensity, and turbulent shear stress in the wake region. In particular, when the turbulence intensity level of the incoming flow is higher, the turbine-induced wake (velocity deficit) recovers faster, and the locations of the maximum turbulence intensity and turbulent stress are closer to the turbine. A detailed analysis of the turbulence kinetic energy budget in the wakes reveals also an important effect of the incoming flow turbulence level on the magnitude and spatial distribution of the shear production and transport terms.

Keywords: atmospheric turbulence; large-eddy simulation; turbulence intensity; turbulence kinetic energy; wind-turbine wakes; wind shear

1. Introduction

Wind turbines operate in the atmospheric boundary-layer (ABL), where they are exposed to different wind speeds, wind shears and turbulence levels, depending on the land/sea surface characteristics,

synoptic forcings and thermal stability conditions. These ABL flow characteristics are known to have important effects on the structure of wind-turbine wake flows, as reported in several studies (comprehensive reviews of turbine-wake research are given by Vermeer *et al.* [1], Hansen *et al.* [2], Sandeise *et al.* [3], and Sørensen [4]). Specifically, ABL turbulence affects two key characteristics of turbine wakes that have received considerable attention in the wind energy community: (a) the velocity deficit, which is directly associated with power losses in wind farms, and (b) the wake turbulence, which affects the flow-induced dynamic loads on downwind turbines. Understanding the aerodynamics of turbine wakes under different incoming ABL flow conditions is, therefore, of great importance to optimize the design (turbine siting) of wind farms, *i.e.*, to maximize the power output and minimize the maintenance costs.

The formation and recovery of turbine wakes are known to be affected by the incoming flow characteristics, the turbine-generated turbulence characteristics, and the operational states of a turbine (e.g., pitch/stall regulation, a yaw condition). In stand-alone turbine wakes, the velocity deficit usually has a two-dimensional Gaussian-like distribution with a maximum located near the turbine hub level. This behaviour is attributed to the increased turbulent mixing induced by the incoming flow [5], and has been shown in both numerical and experimental studies of single turbine wakes in turbulent boundary layer flows [6–8]. The turbulence intensity level in the incoming flow can have a strong effect on the rate of the wake recovery. Evidence also shows that the turbulence level in the incoming flow affects the rate at which this velocity deficit decreases with downwind distance from the turbine (*i.e.*, the wake recovery rate). In particular, both simulations [9–11] and experimental studies [6,12–14] have shown that stand-alone turbine wakes recover faster in conditions of higher turbulence intensity levels in the incoming flows. This effect is found to affect the performance (power output) of the downwind turbines in large wind farms. For example, in the well-known Horns-Rev offshore wind farm [15], the maximum power deficit (with respect to the first row of turbines) of the downwind turbines decreases from 50% to 30% as the turbulence intensity in the incoming flow of the farm increases from 3% to 12% [16]. This result highlights the significant effect of the inflow turbulence on the wake recovery and the total power output from a large wind farm.

The interaction between the wind and a wind turbine induces the formation of a shear layer that starts at the edge of the rotor area and expands downwind. In the case of uniform inflow conditions, this shear layer and the turbulence statistics are axisymmetric, e.g., [10]. However, in the surface layer of the ABL, the non-uniformity of the velocity profile (logarithmic under neutral conditions) leads a non-axisymmetric shear layer, which is stronger at the upper edge of the rotor. This leads to a higher level of shear production of turbulence kinetic energy and, in turn, a more evident enhancement of the turbulence levels in the upper half of the wake. These effects have been reported in recent wind-tunnel [6,7,14,17,18], field [19] and numerical simulation [8,20] studies. The thickness of this shear layer increases with downwind distance and it eventually merges at a distance of about two to five rotor diameters from the turbine, corresponding to the end of the near-wake region. The outer part of the shear layer continues to grow with downwind distance and contributes to the expansion of the turbine wake [21] and, in the case of wind farms, the wind-farm wake [22].

In previous numerical studies of wind-turbine wakes, actuator disk-/line-based methods for modelling rotors have been developed and implemented to simulate the turbine-induced wakes in the context of the

Reynolds-averaged Navier–Stokes (RANS) approach e.g., [23,24] and the large-eddy simulation (LES) technique e.g., [25–27]. Recent validation studies [8,20] have shown that using LES, coupled with the actuator-disk model with rotation (ADM-R), is able to reproduce the magnitude and spatial distribution of the most relevant turbulence statistics (e.g., mean velocity, turbulence kinetic energy and turbulent stresses) of turbine wakes in turbulent boundary layer flows. The ADM-R uses the blade-element momentum (BEM) approach to calculate the lift and drag forces that produce both thrust and rotation, and distributes them over the rotor disk based on the local blade and flow characteristics [8,20,22].

Some numerical studies have addressed the effect that different incoming flow characteristics have on the development of turbine wakes. Rados *et al.* [9] tested several turbine wake models in the context of the RANS-based approach, and compared the results against the measurement of the wakes in the Vindeby offshore wind farm [28]. They indicated that results from all tested models are sensitive to the inflow condition with different turbulence levels in the prediction of the velocity deficit. In particular, turbine wakes recover faster in the flow field with a higher turbulence level. A similar behaviour in the recovery of the velocity deficit was found by Troldborg *et al.* [10] in LESs of stand-alone turbine wakes with both laminar and turbulent uniform inflows. Troldborg *et al.* [26] performed LESs to investigate the wake interaction between two consecutive turbines operating in laminar and turbulent uniform inflow conditions. They showed that the tangential loading, which induces the rotor rotation, increases substantially on the blades of the downstream turbine as the inflow becomes more turbulent. These results highlight the potential of eddy-resolving computational fluid dynamic techniques, and particularly LES, to study the effect of different turbulent inflow conditions on the simulation of wind-turbine wakes. To date, however, no LES study has been performed to systematically investigate how different ABL (non-uniform) inflow conditions change wind-turbine wake characteristics.

In this paper, the effect of atmospheric turbulence on stand-alone turbine wakes is studied using a recently-developed large-eddy simulation (LES) framework. In this framework, a Lagrangian scale-dependent dynamic model is used to parametrize the sub-grid-scale (SGS) stress [29] and an actuator-disk model with rotation (ADM-R) is applied to calculate for the turbine-induced lift and drag forces [8,20]. Numerical experiments are carried out under neutral stability conditions over different types of land surfaces in order to investigate the effect of different incoming boundary-layer flow characteristics on wind-turbine wakes. A short introduction of the LES framework and the numerical set-up are presented in Section 2. The spatial distribution of the mean velocity, the turbulence intensity, and the turbulent shear stress obtained from the turbulence statistics are shown and discussed in Section 3. Finally, a summary is given in Section 4.

2. Large-Eddy Simulations

2.1. LES Framework and Set-up

We use a modified version of the LES code described by Albertson and Parlange [30], Porté-Agel *et al.* [31], Stoll and Porté-Agel [29], Wu and Porté-Agel [8], Porté-Agel *et al.* [20] and Wu and Porté-Agel [22]. The code solves the filtered conservation of mass, and the filtered conservation of momentum in rotation form [32]. The SGS turbulent stress is parametrized using a Lagrangian

scale-dependent dynamic model, which can account for the temporal and spatial variability of the model coefficient based on the resolved flow information without any ad hoc tuning. The numerical algorithm is coded with Fortran 90 and parallelized using a hybrid MPI/OpenMP scheme. The main features of the numerical method can be summarized as follows: It uses a second-order Adams–Bashforth explicit scheme for time advancement and a hybrid pseudospectral finite-difference scheme for the spatial discretization. The spatial derivatives are computed using a high-order pseudospectral scheme in the horizontal directions and a second-order finite-difference approximation in the vertical direction. As a result, the lateral boundary conditions are periodic. The top boundary condition is set up as a flux-free condition. The bottom boundary condition requires the calculation of the instantaneous (filtered) surface shear stress as a function of the velocity field at the lowest vertical grid point, which is accomplished through the local application of Monin–Obukhov similarity theory. It should be noted that, even though similarity theory is strictly valid only for average quantities and over homogeneous surfaces, its application is standard in LES of ABL flows. Both a-priori and a-posteriori studies have shown that some errors can be introduced when using this boundary condition with fluctuating (filtered) quantities e.g., [33,34] and in heterogeneous flows e.g., [35,36]. More details on the numerical method of the LES code can be found in Porté-Agel *et al.* [31], Porté-Agel [37], Stoll and Porté-Agel [34], Stoll and Porté-Agel [29] and Wu and Porté-Agel [8].

The LES code described above has been well tested in neutrally-stratified ABL simulations, in which the turbulence statistics were compared against surface layer similarity theory [29]. Recently, the LES code, coupled with the ADM-R wind-turbine model, has been validated against high-resolution wind-tunnel measurements of the wake flows behind a stand-alone wind turbine [8] and an array of turbines in a wind farm [22]. These validation studies have shown that this LES framework provides reliable simulations of wind-turbine wakes.

To investigate the effect of atmospheric turbulence on wind-turbine wakes, the LES code is used to simulate a series of neutrally-stratified ABL flows through stand-alone wind turbines. The turbines are placed on horizontally-homogeneous flat surfaces with different aerodynamic roughness lengths $z_0 = 0.5, 0.05, 0.005, \text{ and } 0.00005 \text{ m}$. These roughness lengths are representative of different land surface types, including very rough terrain ($z_0 \approx 0.5 \text{ m}$), farmlands ($z_0 \approx 0.05 \text{ m}$), grasslands ($z_0 \approx 0.005 \text{ m}$), and snow-covered flats ($z_0 \approx 0.00005 \text{ m}$) [38]. In the simulations, we adopt a Vestas V80-2MW wind turbine, which has a hub height of $H_{hub} = 70 \text{ m}$ and a rotor diameter of $d = 80 \text{ m}$. To keep a reasonable ratio between the turbine height and the domain height, the simulation domain is set to have a height $L_z = 500 \text{ m}$, corresponding to the boundary-layer depth δ . The horizontal domain spans $L_x = 3000 \text{ m}$ in the streamwise direction and $L_y = 1500 \text{ m}$ in the spanwise direction. The domain is divided uniformly into $N_x \times N_y \times N_z$ grid points with a spatial resolution of $\Delta x \times \Delta y \times \Delta z$ in the streamwise, spanwise and wall normal directions, respectively. Four different spatial resolutions (see Table 1) are used to test the resolution sensitivity of the simulation results. In Table 1, $N_{t,y} = d/\Delta_y$ and $N_{t,z} = d/\Delta_z$ denote the number of grid points covering the rotor diameter in the spanwise and vertical directions, respectively.

To deal with the influence of the turbine-induced wake flow on the incident flow upwind of the turbine due to the periodic boundary conditions, a buffer zone is applied to smoothly adjust the flow from the very-far-wake downwind condition to that of an undisturbed boundary layer inflow condition. First, at

each time step the resolved velocity at the downwind end (outlet) of the buffer zone is replaced with the undisturbed inflow velocity obtained from a separate (without turbine) simulation. The velocity inside the buffer zone is then modified using a cosine smoothing function that allows to retain both the mean and the fluctuations at the inlet and outlet of the buffer zone. The turbine is placed in a location five rotor diameters downstream from the buffer zone. The inflow conditions are obtained from separate simulations of fully-developed neutral ABL flows over horizontally-homogeneous flat surfaces with the four different roughness lengths considered here. More details regarding the separate inflow simulations are discussed in Section 2.2. The use of a similar buffer region to impose the inflow boundary condition while maintaining the accuracy of pseudospectral LES codes has been successful in former studies of turbulent transport in urban street canopies [39], flow over a steep hill [40], flow through a stand-alone wind turbine [8,20], and flows over both aligned and staggered wind farms [22].

Table 1. Numerical set-up for neutrally-stratified ABL simulations with different grid resolutions (GR).

GR cases	N_x	N_y	N_z	Δx (m)	Δy (m)	Δz (m)	$N_{t,y}$	$N_{t,z}$
GR 1	288	192	96	10.42	7.81	5.26	11	16
GR 2	144	90	45	20.83	16.67	11.36	5	7
GR 3	120	72	36	25.00	20.83	14.29	4	6
GR 4	84	54	27	35.71	27.78	19.23	3	4

2.2. Turbine Operating Condition and Inflow Conditions

Based on the operational records of Vestas V80-2MW wind turbines reported by Hansen *et al.* [16], the turbines reach a mean angular velocity of 17.4 rpm when the incoming (upwind) mean wind speed at hub height is $\bar{u}_{hub} \approx 9 \text{ m s}^{-1}$, where the overbar ($\bar{\quad}$) denotes the temporal average. Under this condition, the turbine has a relatively large thrust coefficient ($C_T \approx 0.8$), its blades pitch less than 0.5° within the range $\bar{u}_{hub} \approx 9 \pm 1 \text{ m s}^{-1}$, and the change of the rotor thrust coefficient regulated by the blade pitch is relatively small. Some important parameters regarding the geometry of the V80 turbine blades are available in the literature [41]. For example, the chord length at the blade root and tip positions is 3.52 m and 0.48 m, respectively. The twist angle decreases from 13° (root) to 0° (tip). The V80 blade is composed of a NACA 63-xxx airfoil between the blade tip and its center, and an FFA W3-xxx airfoil between the center of the blade and the hub [42]. Here we use the above-mentioned parameters into the BEM approach [43] and create the radial distribution of the twist angle and the chord length based on the aerodynamic characteristics of the NACA 63-415 and the FFA W3-241 airfoils. In particular, the distribution of both lift and drag coefficients versus the angle of attack can be found in Bak *et al.* [44] for the NACA 63-415 airfoil and in Fuglsang *et al.* [45] for the FFA W3-241 airfoil. The designed blade geometry (*i.e.*, chord length and twist angle) has been tested at different incoming wind speed conditions using the BEM approach, in which the computed total rotor thrust coefficient values show an acceptable agreement with the manufacturer's thrust coefficient curve [46] (see Figure 1).

In this study, the LES code is used to simulate the wakes induced by the wind turbine described above, operating with the same mean angular velocity of 17.4 rpm, in neutral ABL flows developed

over the four different surfaces types, such that the velocity at hub height is the same and has a value of $\bar{u}_{hub} = 9 \text{ m s}^{-1}$. To do this, we calculate the friction velocity u_* based on the log law and the hub-height mean wind speed, and use a streamwise mean pressure gradient force (in kinematic form), $F_p = u_*^2/\delta$, to drive the boundary-layer flow (see Table 2). All the simulations were run for a period (physical time) of 200 min, and the flow statistics were computed during the last 160 min, which guarantees quasi-steady flow conditions as well as statistical convergence of the results presented in the next section.

Figure 1. Manufacturer's and simulated thrust coefficient curves for the Vestas V80-2MW turbine.

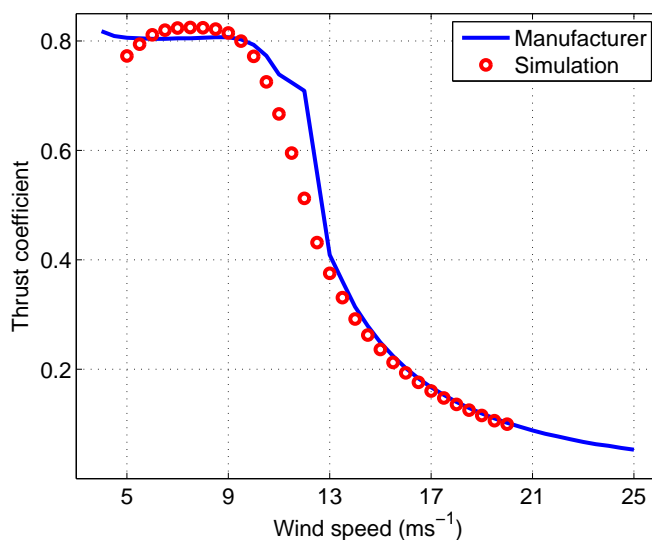


Table 2. Friction velocity and mean streamwise pressure gradient force for simulations of ABL over flat surfaces with four aerodynamic roughness lengths.

ABL cases	z_0 (m)	u_* (m s^{-1})	F_P (m s^{-2})
Case 1	0.5	0.73	1.06×10^{-2}
Case 2	0.05	0.50	4.94×10^{-4}
Case 3	0.005	0.38	2.84×10^{-4}
Case 4	0.00005	0.25	1.29×10^{-4}

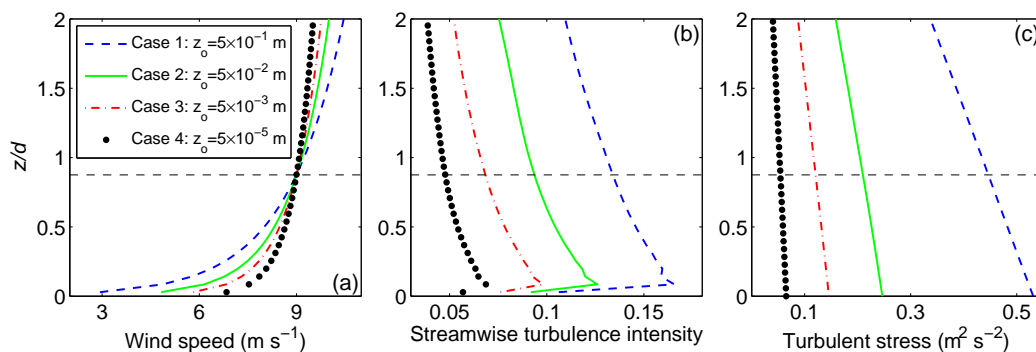
3. Results

3.1. General Turbine Wake Characteristics

In this section, we present results from large-eddy simulations of the wake flows behind wind turbines operating in neutral ABLs over flat surfaces with different roughness lengths ($z_0 = 0.5, 0.05, 0.005,$ and 0.00005 m). These results are obtained from the simulations using the finest grid resolution ($288 \times 192 \times 96$). Spatial distribution of five key turbulence statistics is used to characterize the wind-turbine wakes: time-averaged streamwise velocity \bar{u} (m s^{-1}), normalized velocity deficit $\Delta\bar{u}/\bar{u}_{hub}$,

streamwise turbulence intensity $I_u = \sigma_u / \bar{u}_{hub}$, added turbulence intensity $I_{u,add}$, and kinematic shear stress $-\overline{u'w'}$ ($\text{m}^2 \text{s}^{-2}$). To have the same mean rotating speed on the turbines in all the cases, the upwind incoming flows have the same wind speed $\bar{u}_{hub} = 9 \text{ m s}^{-1}$ at the hub level but different mean wind shears and turbulence intensity levels. Figure 2 displays the main characteristics of the simulated neutrally-stratified ABLs over the different surface types. These simulated velocity fields are then used as inflows to the wind-turbine wake simulations. As expected, the rougher the surface, the higher the shear and, for the same \bar{u}_{hub} , the larger the turbulence intensity and turbulent stresses.

Figure 2. Vertical profiles of (a) the time-averaged streamwise velocity \bar{u} (m s^{-1}); (b) the streamwise turbulence intensity I_u ; and (c) the kinematic shear stress $-\overline{u'w'}$ ($\text{m}^2 \text{s}^{-2}$) of the incoming ABL flows over flat surfaces with the four different roughness lengths.



Figures 3 and 4 display two-dimensional contours of the time-averaged streamwise velocity in a vertical xz plane through the center of the turbines at zero span ($y = 0$) as well as on different yz cross-sectional planes ($x/d = 3, 5, 7, 10,$ and 15) downstream of the turbines, respectively. To further facilitate the quantitative comparison of the results, both lateral and vertical profiles of the normalized velocity deficit $\Delta\bar{u}/\bar{u}_{hub}$ through the center of the wakes are shown in Figure 5 for the same selected downstream locations, where $\Delta\bar{u} = \bar{u}_{inflow} - \bar{u}$ is the time-averaged velocity deficit, and \bar{u}_{inflow} is the time-averaged streamwise inflow velocity shown in Figure 2a. As seen in Figures 3–5, the simulation results indicate that the upwind flows with different mean wind shears and turbulence intensity levels result in significant differences in the mean velocity distribution of the turbine wakes. In general, a higher level of turbulence in the inflow leads to a smaller wake region (*i.e.*, faster wake recovery) due to the increased efficiency of the background ABL turbulence to get mixed with and transfer its momentum into the wake.

In Figure 5, the lateral and vertical profiles of the velocity deficit calculated with respect to the logarithmic incoming wind velocity profiles (shown in Figure 2a) are approximately axisymmetric, with their axes of symmetry located near the turbine axis. This axisymmetric (particularly two-dimensional Gaussian-like) behavior in the turbine wakes is consistent with previous simulation and experimental results by Rados *et al.* [9], Réthoré *et al.* [11], Chamorro and Porté-Agel [6], and Chamorro and Porté-Agel [7]. In Figure 5, it is shown clearly that the radial distribution of the turbine-induced wakes (*i.e.*, the width of the axisymmetric distribution) expands with downstream distance due to the enhanced turbulence mixing. Moreover, due to the presence of the ground surface, the axisymmetry in the vertical

direction breaks down after about 7 rotor diameters, where the size of the turbulent wakes has grown big enough to reach the surface.

Figure 3. Contours of the time-averaged streamwise velocity \bar{u} (m s⁻¹) in the middle vertical plane perpendicular to the turbines installed over flat surfaces with different roughness lengths.

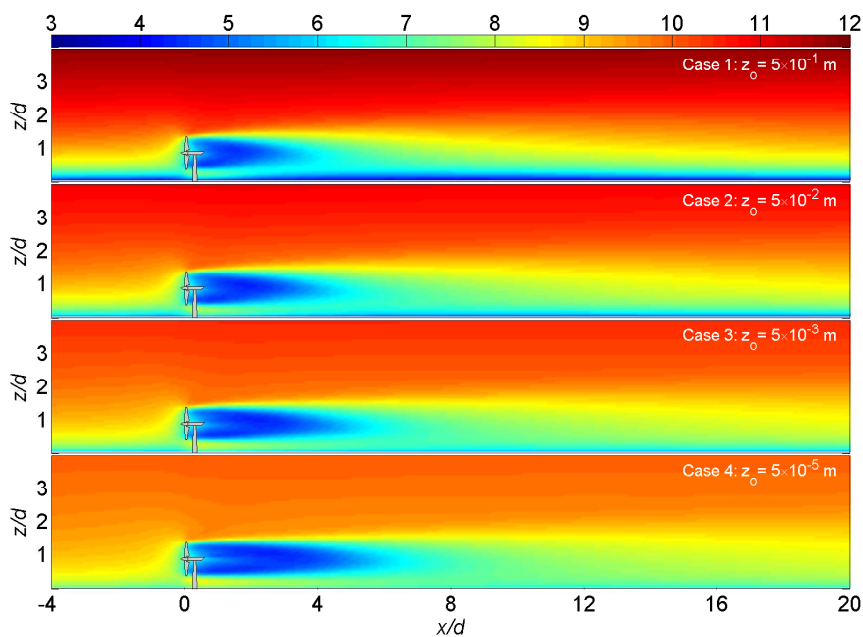


Figure 4. Contours of the time-averaged streamwise velocity \bar{u} (m s⁻¹) at the lateral cross-sectional planes of $x/d = 3, 5, 7, 10,$ and 15 for the turbines installed over flat surfaces with four different roughness lengths. The dotted line denotes the rotor region.

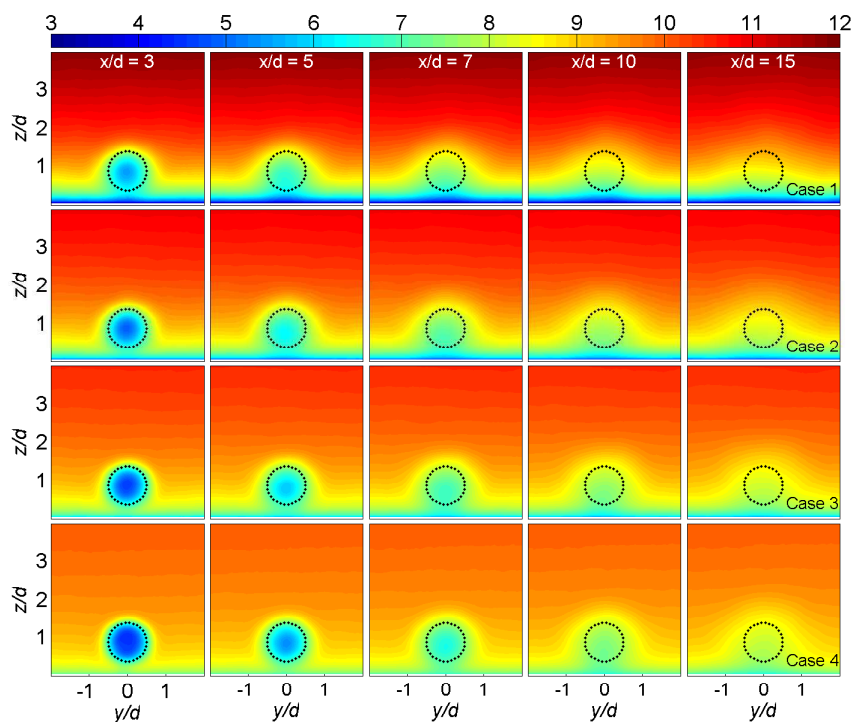
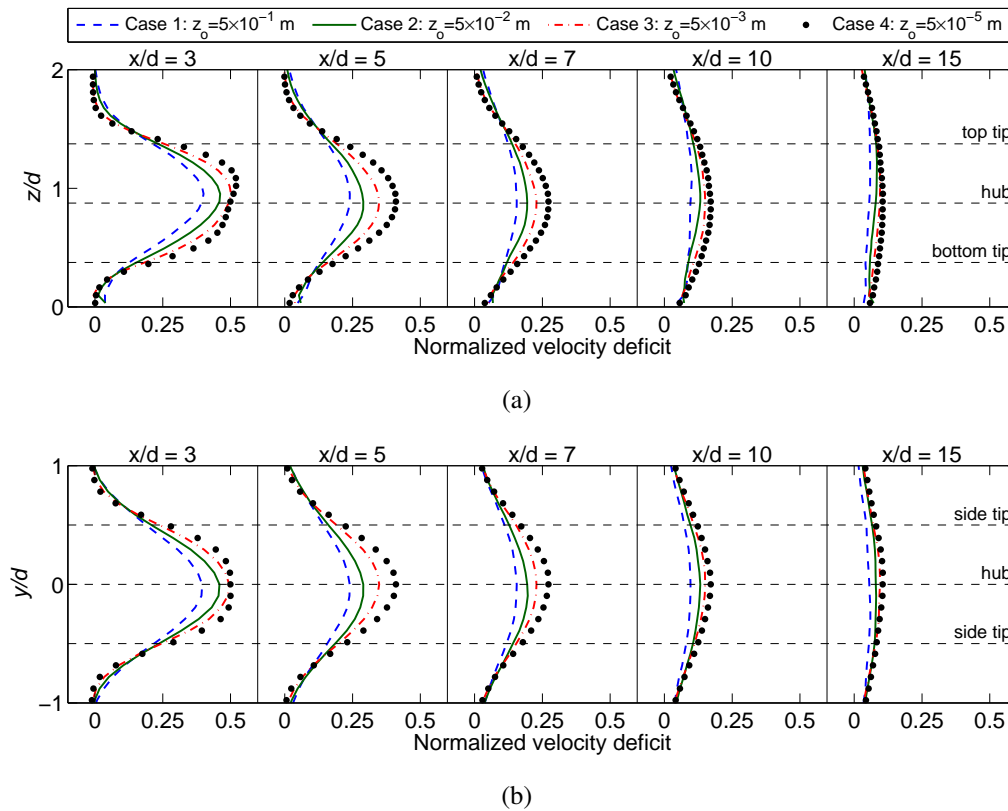


Figure 5. Comparison of vertical (a) and lateral (b) profiles of the normalized velocity deficit $\Delta\bar{u}/\bar{u}_{hub}$ through the hub level of stand-alone turbines installed on flat surfaces with different roughness lengths.



Figures 6 and 7 display two-dimensional contours of the streamwise turbulence intensity in a vertical xz plane through the center of the turbines at zero span ($y = 0$) as well as on different yz cross-sectional planes ($x/d = 3, 5, 7, 10,$ and 15) downstream of the turbines, respectively. From these figures, an obvious enhancement of turbulence intensity is observed in the upper half of the wake. This enhancement is related to intense mechanical production of turbulence kinetic energy associated with the strong shear and momentum flux found at that location. This effect will be further discussed in Section 3.2. It should be noted that, in all the simulations, the maximum turbulence intensity is found at the top-tip level, where the shear is strongest. However, the exact location and magnitude of the maximum turbulence intensity is clearly affected by the inflow condition. In particular, higher turbulence levels in the incoming flow lead to also larger maximum wake turbulence levels, which occur closer to the turbine for the roughest case (about 2 rotor diameters downwind), compared with the smoothest case (about 5 rotor diameters downwind). This is consistent with the faster overall recovery of the wakes observed in the high background turbulence cases.

Turbulence intensity is commonly used as a surrogate measure of the accumulation of fatigue loads on wind turbines. In turbine wakes, the total turbulence intensity I_u is composed of the ambient turbulence intensity $I_{u,inflow}$ from the inflow and the added turbulence $I_{u,add}$ generated by turbines. Here, $I_{u,add}$ is defined as:

$$I_{u,add} = +\sqrt{I_u^2 - I_{u,inflow}^2} \quad I_u \geq I_{u,inflow}, \tag{1}$$

$$I_{u,add} = -\sqrt{I_{u,inflow}^2 - I_u^2} \quad I_u < I_{u,inflow}. \quad (2)$$

Figure 6. Contours of the streamwise turbulence intensity $I_u = \sigma_u/\bar{u}_{hub}$ in the middle vertical plane perpendicular to the turbines installed over flat surfaces with different roughness lengths.

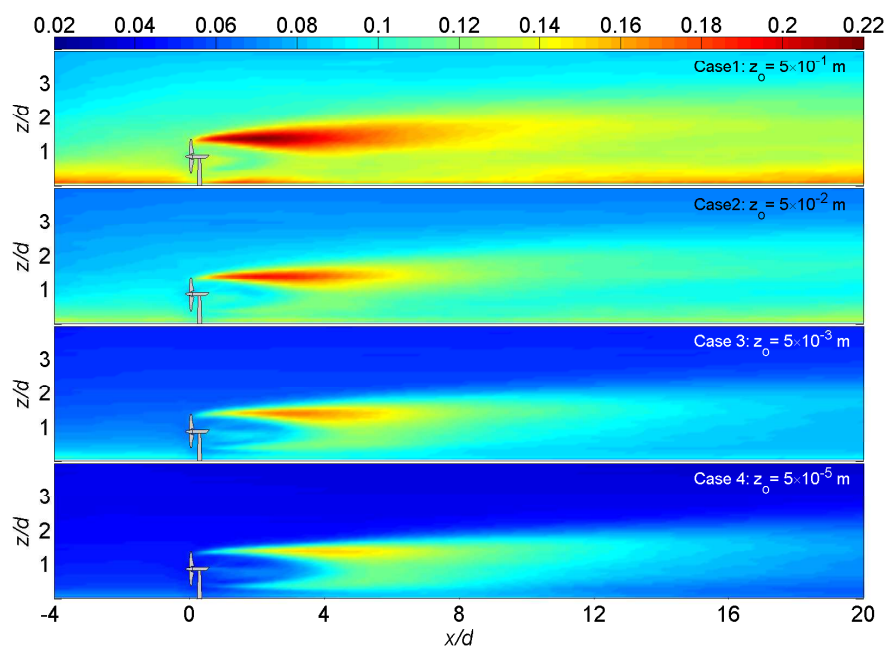
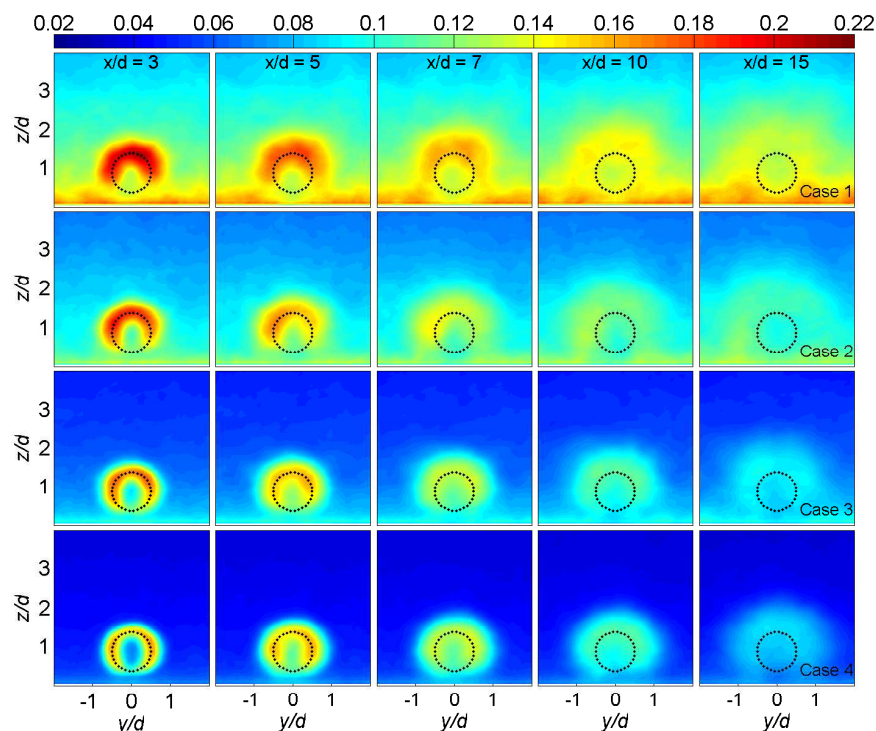


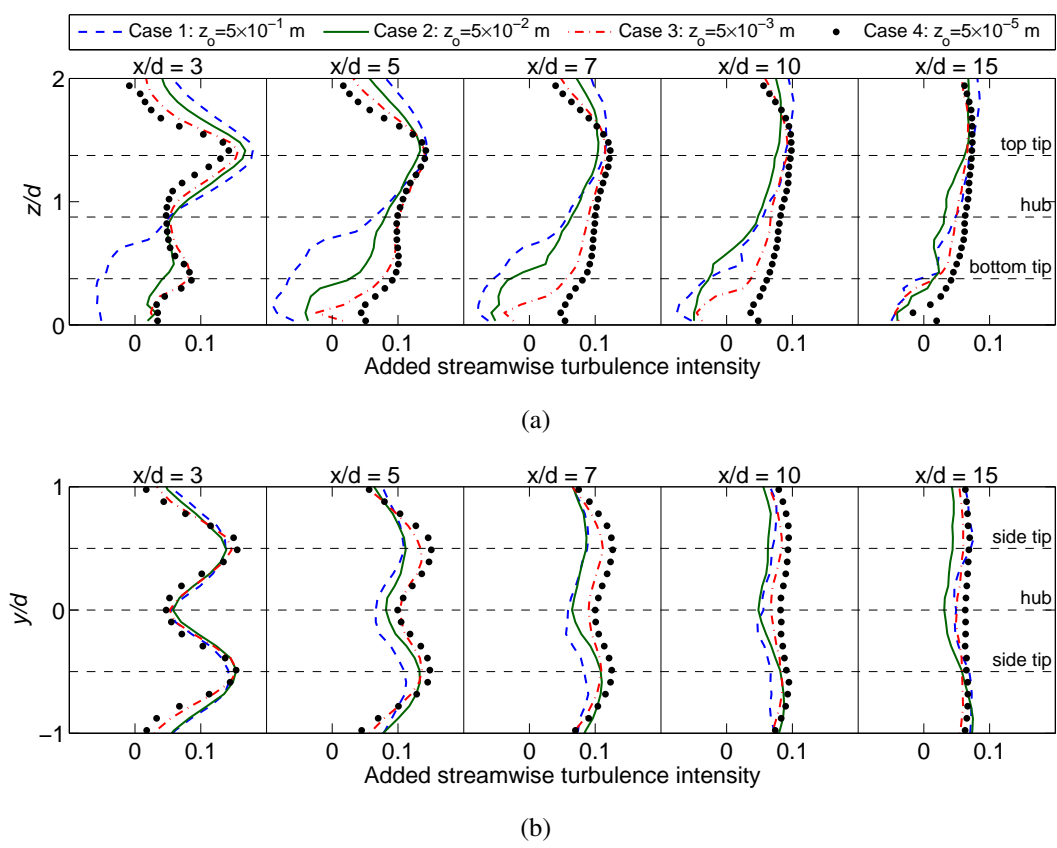
Figure 7. Contours of the streamwise turbulence intensity $I_u = \sigma_u/\bar{u}_{hub}$ at the lateral cross-sectional planes of $x/d = 3, 5, 7, 10,$ and 15 for the turbines installed over flat surfaces with four different roughness lengths. The dotted line denotes the rotor region.



To investigate quantitatively the turbine-induced turbulence, both lateral and vertical profiles of the added turbulence intensity $I_{u,add}$ through the hub of the turbines are shown in Figure 8 at three, five, seven, ten, and fifteen rotor diameters downstream of the turbines. As expected, the magnitude of the added turbulence intensities decreases with respect to downwind distance owing to the turbulent mixing effect. The lateral $I_{u,add}$ profiles exhibit a dual-peak pattern with the larger $I_{u,add}$ values near the two side-tip positions at the hub level. For the selected downstream wake positions, a similar enhancement in the added turbulence intensity appears along the vertical direction, and has the maximum near the top-tip level.

In Figure 8, we find that, below the hub height of the turbines, there is an obvious change in the magnitude of the added turbulence intensity with respect to the four different inflow conditions. In particular, the added turbulence intensity below the hub level becomes smaller as the aerodynamic roughness of the terrain increases. For the roughest terrains, the added turbulence intensity becomes negative in the lower half of the wake, indicating that the wake flow is actually less turbulent than the incoming boundary layer flow at that height. This behavior is consistent with the experimental results reported by Chamorro and Porté-Agel [6] and Zhang *et al.* [14].

Figure 8. Comparison of vertical (a) and lateral (b) profiles of the added streamwise turbulence intensity $I_{u,add}$ through the hub level of the turbines installed on flat surfaces with different roughness lengths.



Figures 9 and 10 display two-dimensional contours of the kinematic shear stress in a vertical xz plane through the center of the turbines at zero span ($y = 0$) as well as on different yz cross-sectional planes ($x/d = 3, 5, 7, 10,$ and 15) downstream of the turbines, respectively. From these figures, it is

evident that the wake flow is associated with a strong enhancement of the turbulence shear stress τ_{xz} , which has positive values around the upper edge of the wake and negative values around the lower edge. This can be explained by the strong entrainment of the surrounding boundary-layer flow into the wake, which produces a momentum flux in the radial direction towards the wake center (hence leading to positive turbulent stress at the upper edge of the wake and negative one at the lower edge). It should be noted that the magnitude of the momentum flux is larger in the upper part of the wake, where the shear is strongest. Like with the turbulence intensity distribution, the higher background turbulence over the rougher surfaces leads to a more axisymmetric wake distribution, with larger values of the wake turbulent stress, compared with the smoother cases. This higher entrainment flux in more turbulent inflow conditions is consistent with the above-described faster wake recovery in those conditions. From Figure 9, the position of the maximum turbulence stress is found near the top-tip level and at a distance downstream of the turbine that ranges from about 2 to 5 rotor diameters, coinciding with the location of the maximum turbulence intensity (Figure 6).

As mentioned earlier, the incoming ABL flows have two important characteristics that can potentially affect the structure of wind-turbine wakes: the ambient turbulence intensity and the mean wind shear. In order to isolate the effect of turbulence intensity from that of wind shear, we have performed an additional simulation using a synthetic inflow velocity field that has the same mean shear as the inflow from Case 1 (roughest surface case) but the turbulence intensity level corresponding to Case 4 (the smoothest surface case). In particular, the synthetic inflow field was constructed by combining the mean velocity profile from the Case 1 inflow with the turbulence velocity fluctuations from the Case 4 inflow. The new simulation case is referred to as Case 5. Vertical profiles of the time-averaged streamwise velocity \bar{u} (m s^{-1}), the streamwise turbulence intensity $I_u = \sigma_u/\bar{u}_{hub}$, and the kinematic shear stress $-\overline{u'w'}$ ($\text{m}^2 \text{s}^{-2}$) for the synthetic inflow velocity field, together with the inflow fields developed over the smoothest (Case 4) and roughest (Case 1) surfaces, are shown in Figure 11.

Figure 9. Contours of the kinematic shear stress τ_{xz} ($\text{m}^2 \text{s}^{-2}$) in the middle vertical plane perpendicular to the turbines installed over flat surfaces with different roughness lengths.

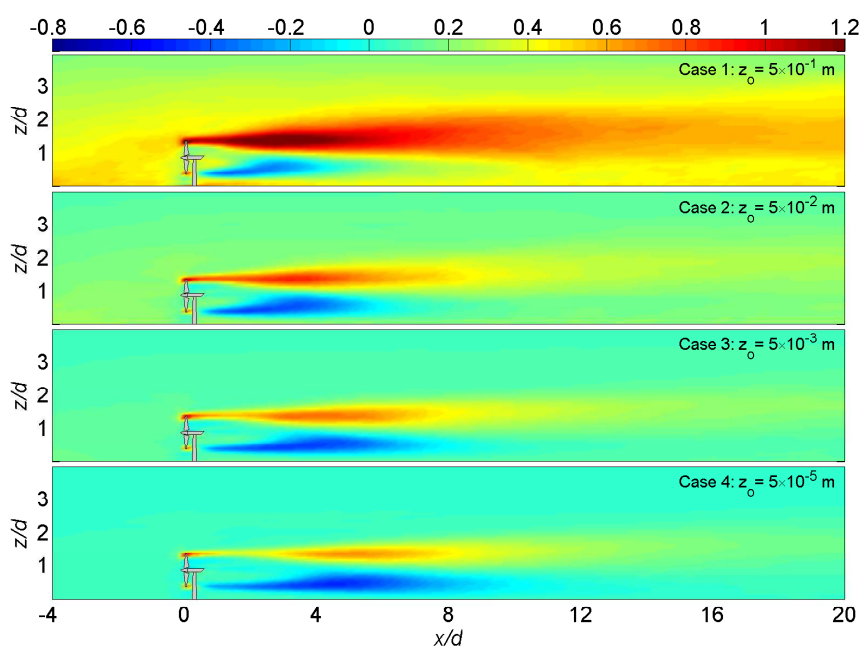


Figure 10. Contours of the kinematic shear stress τ_{xz} ($\text{m}^2 \text{s}^{-2}$) at the lateral cross-sectional planes of $x/d = 3, 5, 7, 10,$ and 15 for the turbines installed over flat surfaces with four different roughness lengths. The dotted line denotes the rotor region.

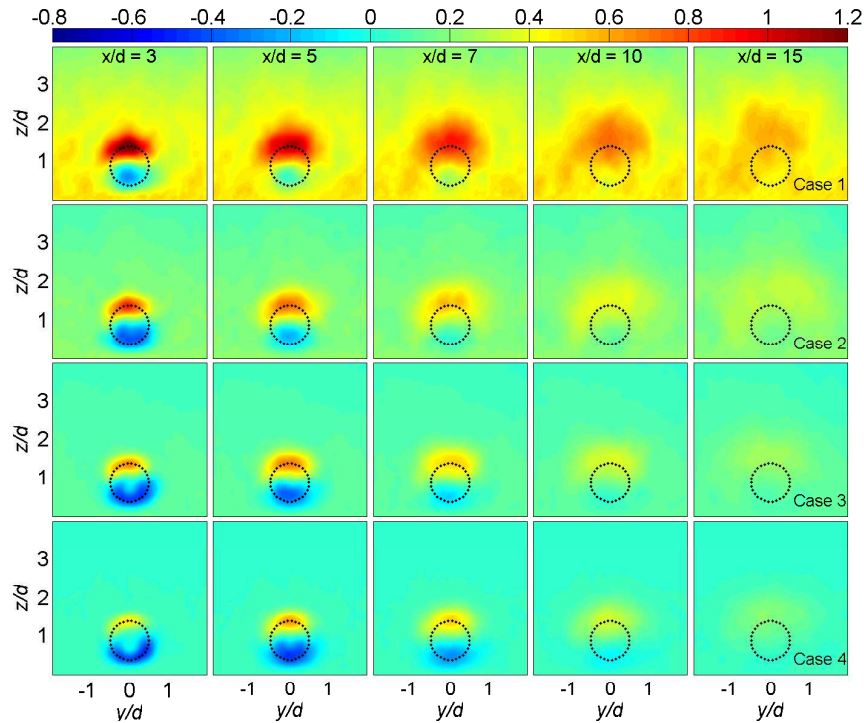
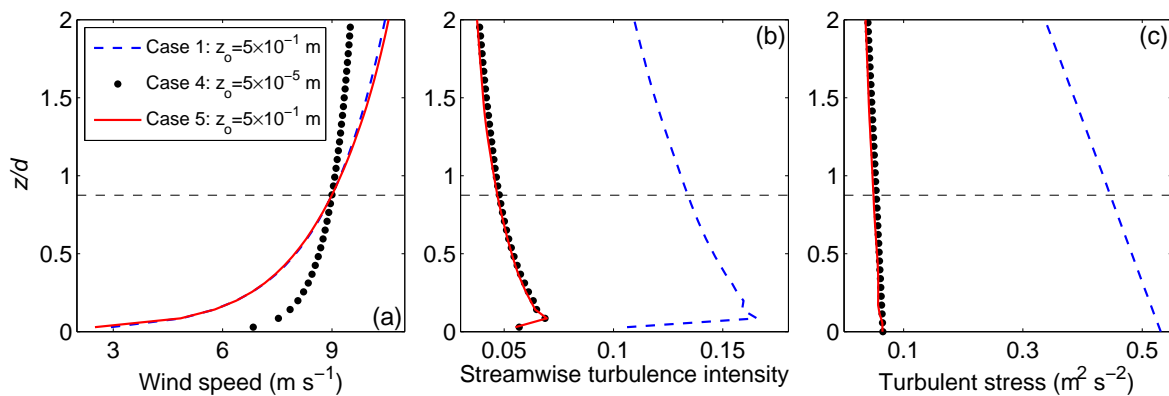


Figure 11. Vertical profiles of (a) the time-averaged streamwise velocity \bar{u} (m s^{-1}); (b) the streamwise turbulence intensity I_u ; and (c) the kinematic shear stress $-\overline{u'w'}$ ($\text{m}^2 \text{s}^{-2}$) of the incoming turbulent boundary layer flows.



Figures 12 and 13 present profiles (spanwise and vertical) of the normalized velocity deficit $\Delta\bar{u}/\bar{u}_{hub}$ and the added streamwise turbulence intensity $I_{u,add}$, respectively, through the center of the wake at selected downwind positions. From these figures, it is evident that turbulence intensity has a stronger effect on the structure and characteristics of wind-turbine wakes, compared with that of the mean wind shear alone. In particular, the higher turbulence levels in the incoming flow facilitate turbulent mixing and entrainment (as reflected in the higher entrainment fluxes and turbulence levels in the wake), which in turn enables the wake velocity to recover faster.

Figure 12. Comparison of vertical (a) and lateral (b) profiles of the normalized velocity deficit $\Delta\bar{u}/\bar{u}_{hub}$ through the centerline of the wakes.

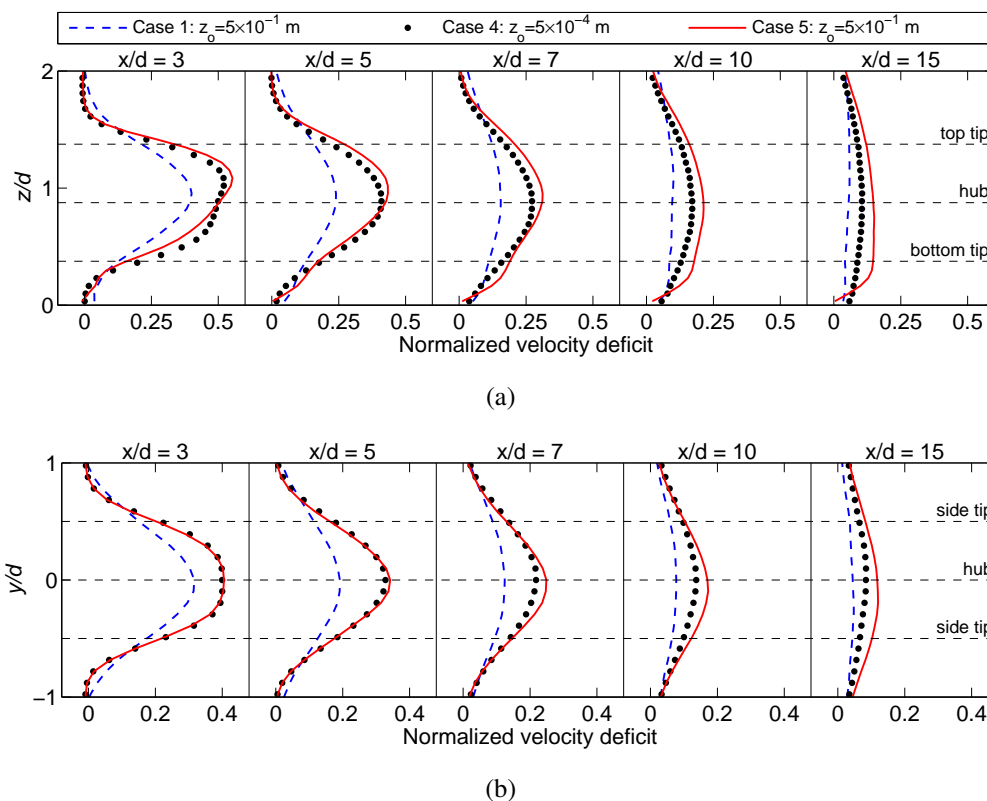
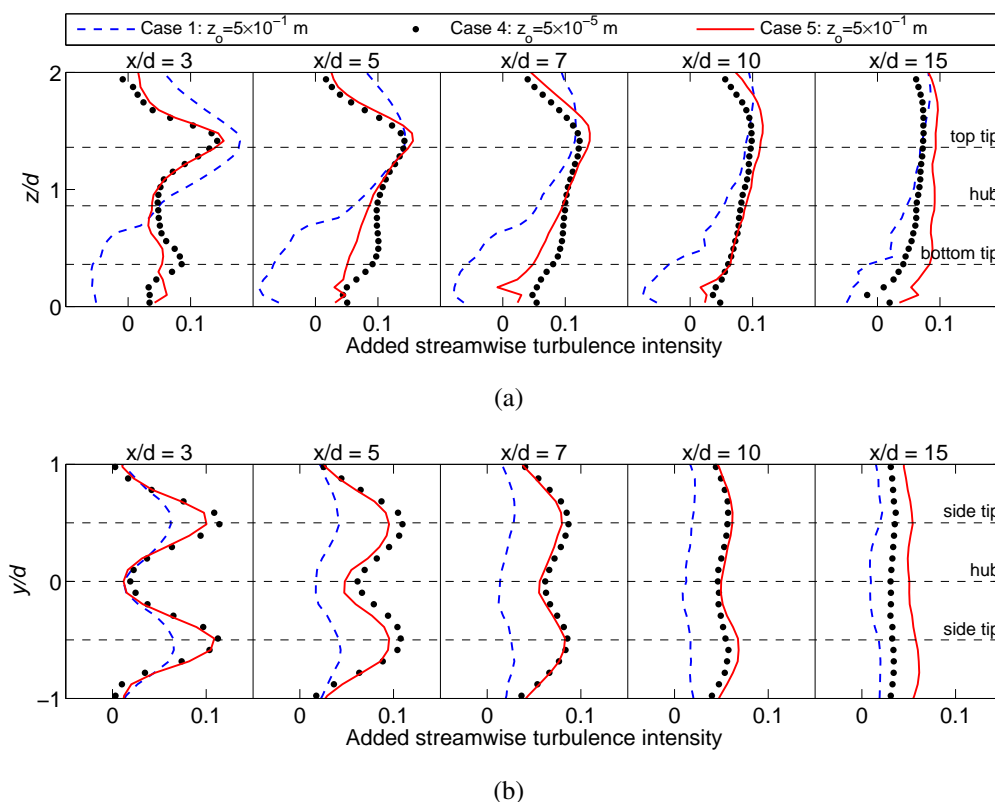
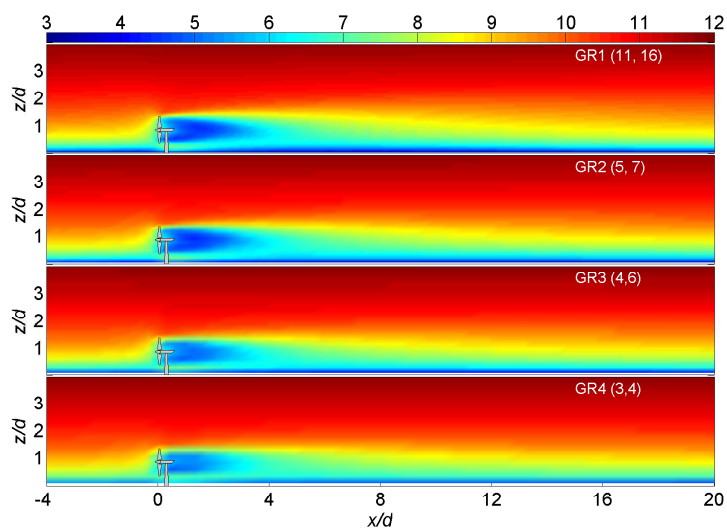


Figure 13. Comparison of vertical (a) and lateral (b) profiles of the added streamwise turbulence intensity $I_{u,add}$ through the centerline of the wakes.

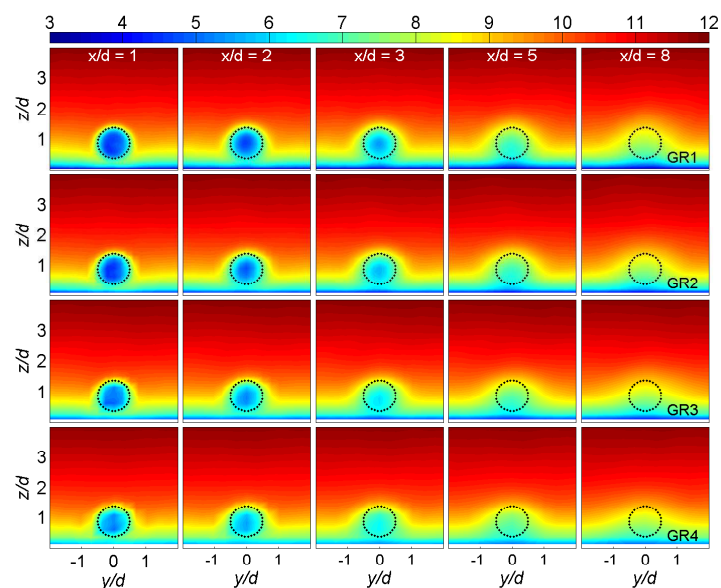


In order to assess the sensitivity of the simulation results to grid resolution, a series of additional simulations were performed of Case 1 with four different grid resolutions (see Table 1). The four cases used a similar grid cell aspect ratio ($\Delta x:\Delta y:\Delta z \approx 1.86:1.46:1.00$). Contour plots of the time-averaged streamwise velocity are shown in Figure 14. To provide a more quantitative comparison of the results obtained with the four grid resolutions, Figures 15 and 16 show the profiles of the normalized velocity deficit and the added streamwise turbulence intensity (resolved part), respectively. The outcome of these resolution sensitivity tests confirms that our recently-developed LES framework yields velocity deficit results that have little resolution dependence as long as at least seven grid points are used to cover the rotor diameter in the vertical direction, and five points in the spanwise direction. This outcome is consistent with the results reported by Wu and Porté-Agel [22] in validations of the same LES framework against wind-tunnel measurements.

Figure 14. Contours of the streamwise velocity obtained from the LESs using different grid resolutions on the xz (a) and yz (b) planes.



(a)



(b)

Figure 15. Comparison of vertical (a) and lateral (b) profiles of the normalized velocity deficit $\Delta \bar{u} / \bar{u}_{hub}$ through the centerline of the wakes.

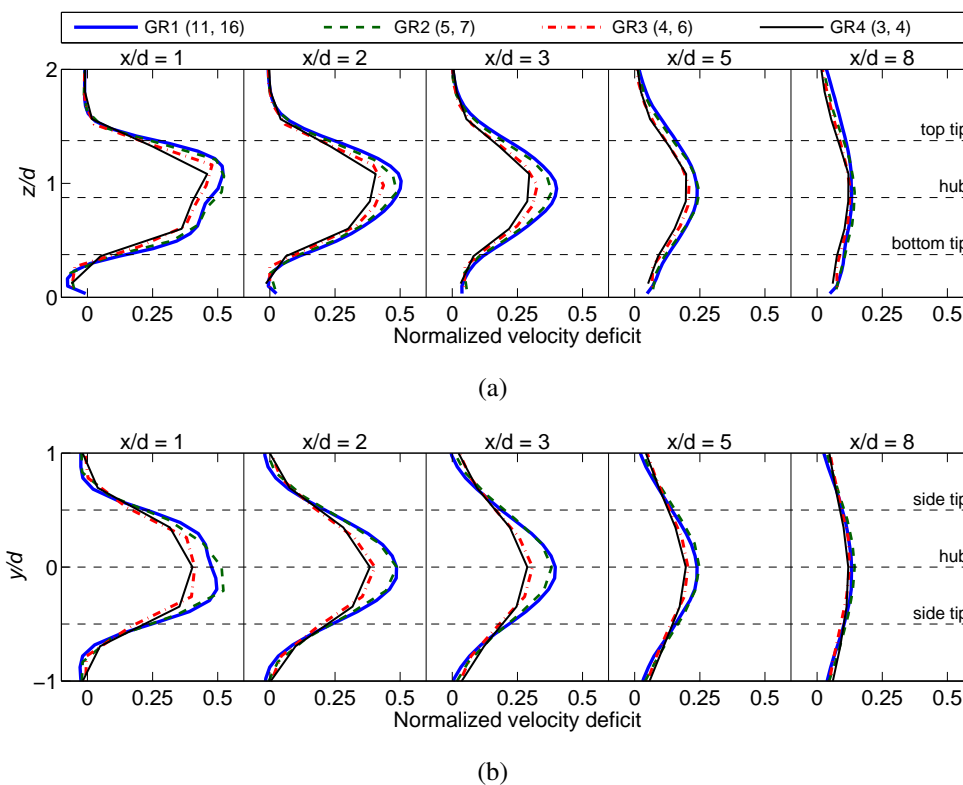
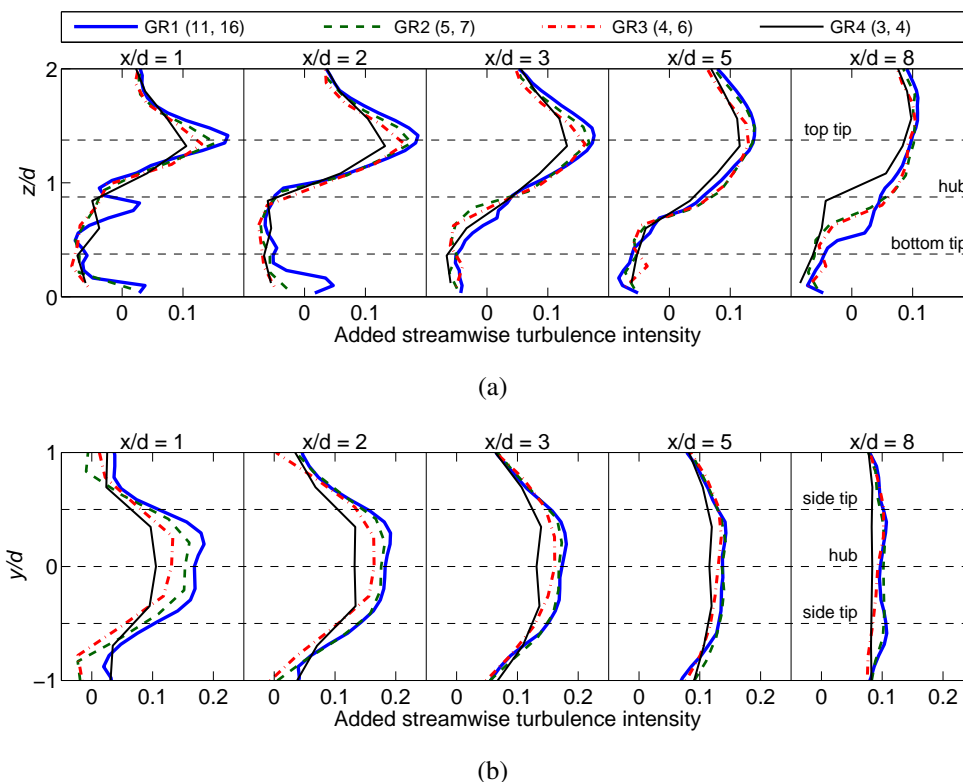


Figure 16. Comparison of vertical (a) and lateral (b) profiles of the added streamwise turbulence intensity $I_{u,add}$ on the xz and xy planes, respectively, through the turbine top-tip level.



3.2. TKE Budget in a Stand-Alone Turbine Wake

Motivated by the simulation results described above, a detailed analysis of the TKE budget is carried out to investigate how the turbine-induced turbulence is produced and transported around in the turbine wakes, and how the different incoming flows affect the relevant mechanisms.

In a neutral condition, the buoyant effect is negligible and the TKE budget equation can be written as follows:

$$\underbrace{\frac{\partial \bar{e}}{\partial t}}_{\substack{\text{Storage} \\ \approx 0}} = - \underbrace{\left[\overline{\tilde{u}'_i \tilde{u}'_j} + \overline{\tau_{ij}^{sgs}} (1 - \delta_{ij}) \right] \frac{\partial \bar{u}_i}{\partial x_j}}_{\text{Shear production}} - \underbrace{\bar{u}_j \frac{\partial \bar{e}_r}{\partial x_j}}_{\text{Advection}} - \underbrace{\frac{\partial \overline{\tilde{u}'_j e_r}}{\partial x_j}}_{\text{Turbulent transport}} + \underbrace{R}_{\text{Residual}} \quad (3)$$

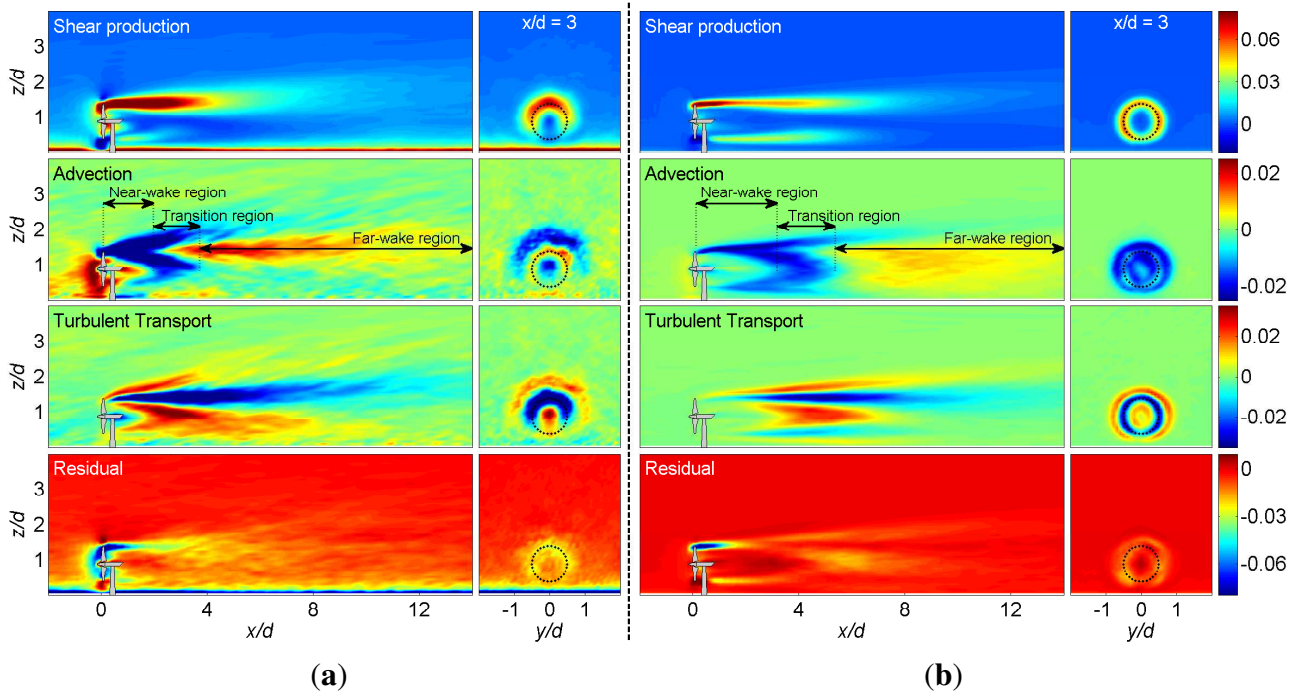
where the overbar ($\bar{}$) denotes the temporal average, the tilde ($\tilde{}$) represents the LES three-dimensional spatial filtering operation at scale Δ , $\bar{e} = 0.5\overline{u_i'^2}$ is the total TKE, $\bar{e}_r = 0.5\overline{u_i'^2}$ is the resolved TKE, \tilde{u}_i is the instantaneous resolved velocity component in the i -direction, \tilde{u}'_i is its fluctuating component, τ_{ij}^{sgs} is the SGS stress, δ_{ij} is the Kronecker delta, and R is the residual term. In Equation (3), the local storage of TKE is close to zero due to quasi-steady flow conditions. Because the SGS stresses are parametrized using the Smagorinsky-based model, the SGS normal stresses (*i.e.*, τ_{xx}^{sgs} , τ_{yy}^{sgs} , τ_{zz}^{sgs}) are not available. Therefore, the residual term includes the contribution of viscous dissipation and pressure-correlation effect as well as some contributions of the SGS turbulence to the production, advection and transport of TKE that cannot be computed from LES data. These later contributions, nonetheless, should be relatively small compared with their resolved counterparts.

Figure 17 shows the contours of the TKE budget terms (shear production, advection, turbulent transport, and residual) in the wake of the turbines operating in two different ABL inflow conditions (Case 1 and Case 4). In the figure, it is obvious that the magnitude of the TKE terms is relatively high in the upper part of the turbine wakes, where the TKE production and transport mechanisms are intense. In particular, the level of the shear production is significant at the rotor tip level. This is consistent with the turbulence intensity results in Figures 6 and 7 which show high values of the turbulence intensity at that same level. This significant turbulence enhancement is associated with the combination of a strong turbulent stress (see Figures 9 and 10) and a large wind shear (see Figure 5) in the turbine-induced shear layer.

As shown in Figure 17, part of the TKE generated at the edge of the turbine wakes (which is stronger in the upper edge) is advected by the mean wind. In particular, the mean advection term is negative in the near-wake region, particularly at top-tip level, due to the positive streamwise gradient of TKE, and it becomes positive after the TKE has reached a maximum and starts to decrease with downwind distance in the far wake. These results indicate that the extent of the near-wake region is affected by the incoming flow turbulence and it is situated approximately two and five rotor diameters from the turbine for the high-turbulence and low-turbulence cases, respectively.

Turbulent transport plays also an important role in redistributing the shear-produced TKE away from the shear layer radially, both inwards and outwards, thus contributing to the expansion of the wake. This explains why the turbulent transport term is negative in the center of the shear layer (around the rotor edge level) and positive on both sides (inside and outside).

Figure 17. Contours of the TKE budget terms (advection, shear production, turbulent transport, and residual) for the stand-alone turbines installed over flat surfaces with the two different roughness lengths: $z_o = 0.5$ m (a panel) and $z_o = 0.00005$ m (b panel). All the quantities are normalized by $u_{hub}^3/\delta = 1.458 \text{ m}^2 \text{ s}^{-3}$.



In Equation (3), the TKE shear production, advection, and turbulent transport terms contain several components. They can be written as follows:

- Shear production

$$\begin{aligned}
 & - \left[\overline{\tilde{u}'_i \tilde{u}'_j} + \overline{\tau_{ij}^{sgs}} (1 - \delta_{ij}) \right] \frac{\partial \tilde{u}_i}{\partial x_j} \\
 & = - \left[\overline{\tilde{u}' \tilde{u}'} \right] \frac{\partial \tilde{u}}{\partial x} \quad - \left[\overline{\tilde{u}' \tilde{v}'} + \overline{\tau_{12}^{sgs}} \right] \frac{\partial \tilde{u}}{\partial y} \quad - \left[\overline{\tilde{u}' \tilde{w}'} + \overline{\tau_{13}^{sgs}} \right] \frac{\partial \tilde{u}}{\partial z} \\
 & \quad - \left[\overline{\tilde{v}' \tilde{u}'} + \overline{\tau_{21}^{sgs}} \right] \frac{\partial \tilde{v}}{\partial x} \quad - \left[\overline{\tilde{v}' \tilde{v}'} \right] \frac{\partial \tilde{v}}{\partial y} \quad - \left[\overline{\tilde{v}' \tilde{w}'} + \overline{\tau_{23}^{sgs}} \right] \frac{\partial \tilde{v}}{\partial z} \\
 & \quad - \left[\overline{\tilde{w}' \tilde{u}'} + \overline{\tau_{31}^{sgs}} \right] \frac{\partial \tilde{w}}{\partial x} \quad - \left[\overline{\tilde{w}' \tilde{v}'} + \overline{\tau_{32}^{sgs}} \right] \frac{\partial \tilde{w}}{\partial y} \quad - \left[\overline{\tilde{w}' \tilde{w}'} \right] \frac{\partial \tilde{w}}{\partial z} \\
 & = P^{(1,1)} \quad + P^{(1,2)} \quad + P^{(1,3)} \\
 & + P^{(2,1)} \quad + P^{(2,2)} \quad + P^{(2,3)} \\
 & + P^{(3,1)} \quad + P^{(3,2)} \quad + P^{(3,3)} \tag{4}
 \end{aligned}$$

- Advection

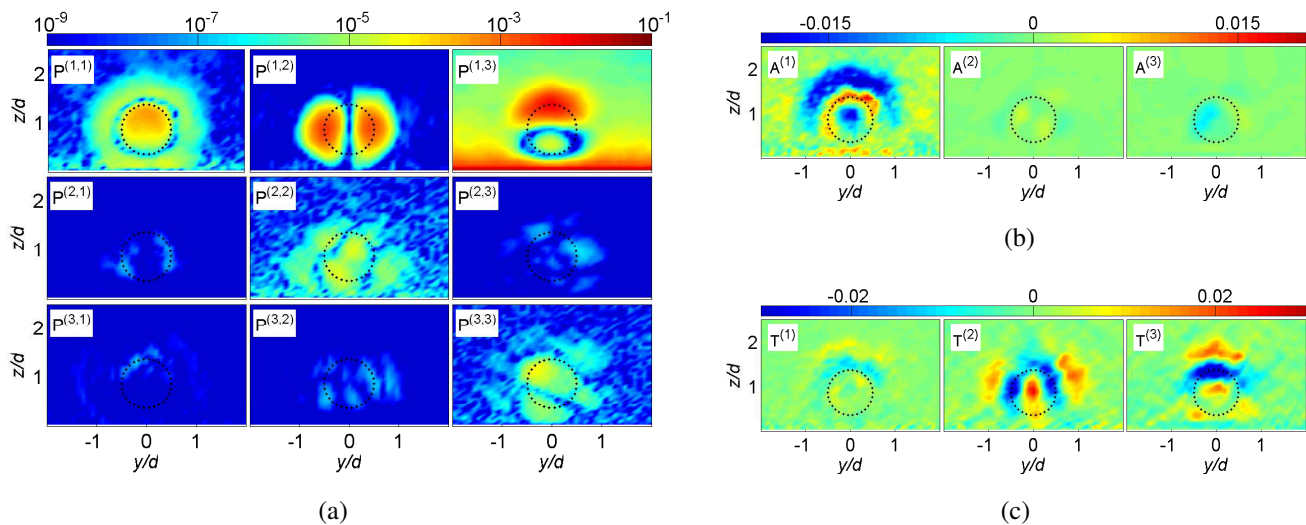
$$-\tilde{u}_j \frac{\partial \tilde{e}_r}{\partial x_j} = -\tilde{u} \frac{\partial \tilde{e}_r}{\partial x} \quad -\tilde{v} \frac{\partial \tilde{e}_r}{\partial y} \quad -\tilde{w} \frac{\partial \tilde{e}_r}{\partial z} = A^{(1)} + A^{(2)} + A^{(3)} \tag{5}$$

- Turbulent transport

$$-\frac{\partial \overline{\tilde{u}'_j e_r}}{\partial x_j} = -\frac{\partial \overline{\tilde{u}' e_r}}{\partial x} - \frac{\partial \overline{\tilde{v}' e_r}}{\partial y} - \frac{\partial \overline{\tilde{w}' e_r}}{\partial z} = T^{(1)} + T^{(2)} + T^{(3)} \quad (6)$$

In order to investigate the relative importance of the above components to the TKE budget, Figure 18 shows the contours of these components at the lateral cross-sectional plane of $x/d = 3$ for the turbine installed over the roughest surface (*i.e.*, Case 1). From this figure, it is evident that most of the TKE in the wake is generated by two components: $-\overline{\tilde{u}'\tilde{v}'\frac{\partial \tilde{u}}{\partial y}}$ and $-\overline{\tilde{u}'\tilde{w}'\frac{\partial \tilde{u}}{\partial z}}$. This is consistent with the high shear of the mean velocity in the radial direction (and thus in the vertical and spanwise directions), and the strong associated radial fluxes of momentum (towards the center of the wake). As for the TKE transport mechanisms, it is clear that part of the TKE in the wake is advected by the streamwise component of the mean wind due to the fact that \tilde{u} is much larger than \tilde{v} and \tilde{w} . In the turbulent transport, it is dominated by $T^{(2)}$ and $T^{(3)}$ because the spanwise and vertical velocity fluctuations (\tilde{v}' and \tilde{w}') are responsible for the radial transport of TKE.

Figure 18. Contours of the components of the TKE budget terms at the lateral cross-sectional plane of $x/d = 3$ for the turbine installed over the roughest flat surface. (a) shear production; (b) advection; and (c) turbulent transport.



4. Conclusions

A series of numerical experiments were carried out to study the effect of atmospheric turbulence on stand-alone wind-turbine wakes. Large-eddy simulations of neutral atmospheric boundary layers over flat surfaces with different aerodynamic roughness lengths $z_0 = 0.5, 0.05, 0.005,$ and 0.00005 m were performed to investigate the characteristics of wind-turbine wakes in cases where the incident flows to the wind turbine have the same mean velocity at the hub height but different mean wind shears and turbulence intensity levels. These roughness lengths considered in this study are representative of land surface types, including very rough terrain ($z_0 \approx 0.5$ m), farmlands ($z_0 \approx 0.05$ m), grasslands ($z_0 \approx 0.005$ m), and snow-covered flats ($z_0 \approx 0.00005$ m) [38].

The simulation results show that the different wind shears and turbulence intensity levels of the incoming flow lead to substantial differences in the spatial distribution of the mean velocity deficit,

turbulence intensity, and turbulent shear stress in the turbine wakes. Overall, the higher turbulence levels of the incoming ABL flow over rougher terrain lead to higher turbulent entrainment fluxes into the wake and, consequently, a faster wake recovery, compared with the less turbulent flows over the smoother surfaces. In all cases, the highest turbulent fluxes and turbulence intensity levels in the wake are found around the upper edge of the wake, and particularly at top-tip level, where the mean shear is maximum. Specifically, the maximum turbulence intensity and fluxes are detected at a downwind distance that ranges from approximately 2 to 5 rotor diameters for the roughest and the smoothest cases, respectively. The non-axisymmetry of the wake is found to be smaller for the roughest conditions. Under those conditions, the added turbulence in the wake (with respect to the turbulence level of the incoming flow) is positive above the hub height, but negative below. Detailed analysis of the TKE budget reveals that TKE production reaches a peak also around the upper edge of the wake, due to the high shear and turbulent fluxes in that region. The TKE is mainly redistributed by both mean-wind advection and turbulent transport in the axial and radial directions, respectively. Besides, the different inflow conditions result in a substantial change in the magnitude of the added turbulence intensity below the hub level, where its value decreases from positive to negative as the turbine wakes are developed over flat surfaces with a smooth roughness length to a rough one.

In order to isolate the effect of turbulence intensity from that of the mean shear, an additional simulation was performed using a synthetic inflow velocity field that has the same mean velocity as the inflow of the above-described roughest case, but the turbulence (velocity fluctuations) corresponding to the smoothest case. Our results reveal that turbulence intensity has a stronger effect on the structure and characteristics of wind-turbine wakes (e.g., spatial distribution of velocity deficit and turbulence intensity) than that of the mean wind shear. Besides, resolution sensitivity analysis shows that the mean velocity results have very little resolution dependence as long as at least seven grid points are used across the rotor diameter in the vertical direction, and five points in the spanwise direction. This outcome is consistent with the results obtained using the same LES framework by Wu and Porté-Agel [22].

Future research will focus on the investigation of the structure and characteristics of the wakes originated from large wind farms under different ABL flow cases involving different land-surface covers and different atmospheric stability conditions.

Acknowledgements

This research was supported by the Swiss National Science Foundation (Grant 200021_132122), and the National Science Foundation (Grants EAR-0537856 and ATM-0854766). Computing resources were provided by the Minnesota Supercomputing Institute, and the Swiss National Supercomputing Centre under project ID s306.

References

1. Vermeer, L.J.; Sørensen, J.N.; Crespo, A. Wind turbine wake aerodynamics. *Prog. Aerosp. Sci.* **2003**, *39*, 467–510.
2. Hansen, M.O.L.; Sørensen, J.N.; Voutsinas, S.; Sørensen, N.; Madsen, H.A. State of the art in wind turbine aerodynamics and aeroelasticity. *Prog. Aerosp. Sci.* **2006**, *42*, 285–330.

3. Sanderse, B.; van der Pijl, S.P.; Koren, B. Review of computational fluid dynamics for wind turbine wake aerodynamics. *Wind Energy* **2011**, *14*, 799–819.
4. Sørensen, J.N. Aerodynamic aspects of wind energy conversion. *Annu. Rev. Fluid Mech.* **2011**, *43*, 427–448.
5. Troldborg, N. Actuator Line Modeling of Wind Turbine Wakes. Ph.D. Thesis, Technical University of Denmark, Lyngby, Denmark, 2008.
6. Chamorro, L.; Porté-Agel, F. A wind-tunnel investigation of wind-turbine wakes: Boundary-layer turbulence effects. *Bound. Layer Meteorol.* **2009**, *132*, 129–149.
7. Chamorro, L.; Porté-Agel, F. Effects of thermal stability and incoming boundary-layer flow characteristics on wind-turbine wakes: A wind-tunnel study. *Bound. Layer Meteorol.* **2010**, *136*, 515–533.
8. Wu, Y.T.; Porté-Agel, F. Large-eddy simulation of wind-turbine wakes: Evaluation of turbine parametrisations. *Bound. Layer Meteorol.* **2011**, *138*, 345–366.
9. Rados, K.; Larsen, G.; Barthelmie, R.; Schlez, W.; Lange, B.; Schepers, G.; Hegberg, T.; Magnisson, M. Comparison of wake models with data for offshore windfarms. *Wind Eng.* **2001**, *25*, 271–280.
10. Troldborg, N.; Sørensen, J.N.; Mikkelsen, R. Actuator line simulation of wake of wind turbine operating in turbulent inflow. *J. Phys. Conf. Ser.* **2007**, *75*, 012063.
11. Réthoré, P.E.; Sørensen, N.N.; Bechmann, A.; Zahle, F. Study of the atmospheric wake turbulence of a CFD actuator disc model. In *Proceedings of European Wind Energy Conference*, Marseille, France, 16–19 March 2009.
12. Medici, D.; Alfredsson, P. Measurement on a wind turbine wake: 3D effects and bluff body vortex shedding. *Wind Energy* **2006**, *9*, 219–236.
13. Maeda, T.; Kamada, Y.; Murata, J.; Yonekura, S.; Ito, T.; Okawa, A.; Kogaki, T. Wind tunnel study on wind and turbulence intensity profiles in wind turbine wake. *J. Therm. Sci.* **2011**, *20*, 127–132.
14. Zhang, W.; Markfort, C.D.; Porté-Agel, F. Near-wake flow structure downwind of a wind turbine in a turbulent boundary layer. *Exp. Fluids.* **2012**, *52*, 1219–1235.
15. Vattenfall-Dong energy Website. Available online: <http://www.hornsrev.dk/index.en.html> (accessed on 13 December 2012).
16. Hansen, K.S.; Barthelmie, R.J.; Jensen, L.E.; Sommer, A. The impact of turbulence intensity and atmospheric stability on power deficits due to wind turbine wakes at Horns Rev wind farm. *Wind Energy* **2012**, *15*, 183–196.
17. Zhang, W.; Markfort, C.D.; Porté-Agel, F. Wind-turbine wakes in a convective boundary layer: A wind-tunnel study. *Bound. Layer Meteorol.* **2013**, doi: 10.1007/s10546-012-9751-4.
18. Markfort, C.D.; Zhang, W.; Porté-Agel, F. Turbulent flow and scalar transport through and over aligned and staggered wind farms. *J. Turbul.* **2012**, *13*, 1–36.
19. Iungo, V.G.; Wu, Y.T.; Porté-Agel, F. Field measurements of wind turbine wakes with LiDARs. *J. Atmos. Ocean. Technol.* **2013**, doi: 10.1175/JTECH-D-12-00051.1.
20. Porté-Agel, F.; Wu, Y.T.; Lu, H.; Conzemius, R.J. Large-eddy simulation of atmospheric boundary layer flow through wind turbines and wind farms. *J. Wind Eng. Ind. Aerodyn.* **2011**, *99*, 154–168.

21. Troldborg, N.; Sørensen, J.N.; Mikkelsen, R. Numerical simulations of wake characteristics of a wind turbine in uniform inflow. *Wind Energy* **2010**, *13*, 86–99.
22. Wu, Y.T.; Porté-Agel, F. Simulation of turbulent flow inside and above wind farms: Model validation and layout effects. *Bound. Layer Meteorol.* **2013**, doi: 10.1007/s10546-012-9757-y.
23. Gómez-Elvira, R.; Crespo, A.; Migoya, E.; Manuel F. Hernández, J. Anisotropy of turbulence in wind turbine wakes. *J. Wind Eng. Ind. Aerodyn.* **2005**, *93*, 797–814.
24. Kasmi, A.E.; Masson, C. An extended κ - ϵ model for turbulent flow through horizontal-axis wind turbines. *J. Wind Eng. Ind. Aerodyn.* **2008**, *96*, 103–122.
25. Jimenez, A.; Crespo, A.; Migoya, E.; Garcia, J. Application of a LES technique to characterize the wake deflection of a wind turbine in yaw. *Wind Energy* **2010**, *13*, 559–572.
26. Troldborg, N.; Larsen, G.C.; Madsen, H. A., H.K.S.; Sørensen, J.N.; Mikkelsen, R. Numerical simulations of wake interaction between two wind turbines at various inflow conditions. *Wind Energy* **2011**, *14*, 859–876.
27. Lu, H.; Porté-Agel, F. Large-eddy simulation of a very large wind farm in a stable atmospheric boundary layer. *Phys. Fluids* **2011**, *23*, 065101.
28. 4C Offshore. Available online: <http://www.4coffshore.com/windfarms/ravnsborg-denmark-dk06.html> (accessed on 13 December 2012).
29. Stoll, R.; Porté-Agel, F. Dynamic subgrid-scale models for momentum and scalar fluxes in large-eddy simulations of neutrally stratified atmospheric boundary layers over heterogeneous terrain. *Water Resour. Res.* **2006**, *42*. W01409.
30. Albertson, J.D.; Parlange, M.B. Surface length scales and shear stress: Implications for land-Atmosphere interactions over complex terrain. *Water Resour. Res.* **1999**, *35*, 2121–2132.
31. Porté-Agel, F.; Meneveau, C.; Parlange, M.B. A scale-dependent dynamic model for large-eddy simulations: Application to a neutral atmospheric boundary layer. *J. Fluid. Mech.* **2000**, *415*, 261–284.
32. Orszag, S.A.; Pao, Y.H. Numerical computation of turbulent shear flows. *Adv. Geophys.* **1975**, *18A*, 225–236.
33. Marusic, I.; Kunkel, G.J.; Porté-Agel, F. Experimental study of wall boundary conditions for large-eddy simulation. *J. Fluid. Mech.* **2001**, *446*, 309–320.
34. Stoll, R.; Porté-Agel, F. Effect of roughness on surface boundary conditions for large-eddy simulation. *Bound. Layer Meteorol.* **2006**, *118*, 169–187.
35. Chamorro, L.; Porté-Agel, F. Wind-tunnel study of surface boundary conditions for large-eddy simulation of turbulent flow past a rough-to-smooth surface transition. *J. Turbul.* **2010**, *11*, 1–17.
36. Abkar, M.; Porté-Agel, F. A new boundary condition for large-eddy simulation of boundary-layer flow over surface roughness transitions. *J. Turbul.* **2012**, *13*, 1–18.
37. Porté-Agel, F. A scale-dependent dynamic model for scalar transport in large-eddy simulations of the atmospheric boundary layer. *Bound. Layer Meteorol.* **2004**, *112*, 81–105.
38. Stull, R.B. *An Introduction to Boundary Layer Meteorology*; Springer: New York, NY, USA, 1988.
39. Tseng, Y.; Meneveau, C.; Parlange, M.B. Modeling flow around bluff bodies and predicting urban dispersion using large eddy simulation. *Environ. Sci. Technol.* **2006**, *40*, 2653–2662.

40. Wan, F.; Porté-Agel, F. Large-eddy simulation of stably-stratified flow over a steep hill. *Bound. Layer Meteorol.* **2011**, *138*, 367–384.
41. *Technical Description of the Wind Farm Project*; EPA: Vienna, Austria, 2004.
42. Ilinca, A. Analysis and Mitigation of Icing Effects on Wind Turbines. In *Wind Turbines*; Al-Bahadly, I., Ed.; InTech: Rijeka, Croatia, 2011; ISBN: 978-953-307-221-0. Available online: <http://www.intechopen.com/books/wind-turbines/analysis-and-mitigation-of-icing-effects-on-wind-turbines> (accessed on 13 December 2012).
43. Manwell, J.; McGowan, J.; Rogers, A. *Wind Energy Explained: Theory, Design and Application*; Wiley: New York, NY, USA, 2002; pp. 134–138.
44. Bak, C.; Fuglsang, P.; Johansen, J.; Antoniou, I. *Wind Tunnel Tests of the NACA 63-415 and a Modified NACA 63-415 Airfoil*; Risø National Laboratory: Roskilde, Denmark, 2000; Risø-R-1193, pp. 1–108.
45. Fuglsang, P.; Antoniou, I.; Dahl, K.S.; Madsen, H.A. *Wind Tunnel Tests of the FFA-W3-241, FFA-W3-301 and NACA 63-430 Airfoils*; Risø National Laboratory: Roskilde, Denmark, 1998; Risø-R-1041, pp. 1–163.
46. Jensen, L.; Mørch, C.; Sørensen, P.B.; Svendsen, K. Wake measurements from the Horns Rev wind farm. In *Proceedings of European Wind Energy Conference*, London, UK, 22–25 November 2004.

© 2012 by the authors; licensee MDPI, Basel, Switzerland. This article is an open access article distributed under the terms and conditions of the Creative Commons Attribution license (<http://creativecommons.org/licenses/by/3.0/>).